L-arginine-etched nickel-silver electrocatalyst for low-potential hydrogen evolution

Yan Zhang [a], Jindong Wu [a], Xinrui Zhu [a], Zhi Ren [b,*], Jiean Chen [a,*]

[a] *Pingshan Translational Medicine Center, Shenzhen Bay Laboratory, Shenzhen 518055, China*
[b] *College of Pharmacy, Shenzhen Technology University, Shenzhen 518055, China*

ARTICLE INFO

ABSTRACT

The oxidation of formaldehyde at low potentials to achieve anodic hydrogen production is a crucial focus of current research. Copper-based alloys are prominent electrocatalysts in these reactions but face long-term stability challenges and are susceptible to CO intermediate poisoning. A novel approach that utilizes L-arginine in the surface modification of nickel foam substrates has been developed, enabling the highly dispersed deposition of silver catalysts on the substrates as sub-nanometer particles. This modified electrocatalyst allows formaldehyde oxidation and water electrolysis at a minimal potential of 0.32 V_{RHE} and bipolar hydrogen production with near 100% Faradaic efficiency. This surface modification of substrate material provides a new approach to the design of electrodes.

1. Introduction

In recent years, the increasing power generation capacity of nuclear, wind, hydropower and other renewable energy sources has resulted intermittently in surplus electricity [1–4]. Consequently, efficient storage of excess electric energy becomes essential for rational allocation of energy resources. Hydrogen has attracted considerable interest as the most energy-efficient chemical and a promising alternative to fossil fuels, and various production methods are being explored to meet the future demand for hydrogen [5–7]. Among these, electrolysis of water is an attractive method because it uses water as a raw material and produces a clean end product [8–10]. "Peak shaving" and "valley filling" of electrical power can be implemented by converting surplus electrical energy into hydrogen by electrolysis of water. This allows excess energy to be stored as hydrogen and used for high electricity demand. However, a significant challenge for the development and application of water electrolysis is the high theoretical potential (1.23 V *vs.* hydrogen evolution reaction, HER) of the anodic oxygen evolution reaction (OER) [11–16]. This leads to several problems, such as oxygen-hydrogen mixing, cost and complexity in the separation and the risk of explosions during transportation. Developing a coupling mechanism between oxidation reactions and HERs that can operate at lower potentials is a critical research issue that can address the current energy dilemma and overcome the scientific challenges. This research aims to achieve this

goal and seeks potential solutions.

Anodic oxidation of small organic molecules, such as methanol [17, 18], formic acid [19], 5-hydroxymethylfurfural [20,21], urea [22,23] and hydrazine [24,25], can feasibly replace the OER and reduce the overpotential. This method can lower the oxidation potential significantly and decrease the energy consumption during electrolysis of water, producing hydrogen [26,27]. Additionally, it offers potential benefits in terms of efficiency and energy savings [28]. Significant advancements have been made in recent years in studying biomass-derived furfural compounds. Particularly noteworthy is the utilization of aldehyde compounds to generate hydrogen simultaneously at both the anode and cathode through water electrolysis [29,30]. Meanwhile, attention has shifted towards formaldehyde, the simplest aldehyde compound. Recently, coupling a formaldehyde oxidation reaction (FOR) with HER at the anode has been shown to produce hydrogen at a lower potential [26,27]. This method avoids the separation challenges and explosion risks of hydrogen and oxygen mixtures, as formaldehyde is oxidized, producing hydrogen and formate derivatives. Pan et al [26]. have shown that Cu-based materials are among the most promising candidates for FORs due in part to their low cost, but the long-term stability of materials under high current density is still a challenging issue. Li et al [27]. reported a bimetallic species, Cu_3Ag_7, as an efficient electrocatalyst, revealing the importance of both Ag and Cu in the FOR process. The energetic profiles show the advantages of Ag over Cu in C-H cleavage of

---

the essential $H_2C(OH)O*$ intermediate, as in the Tafel recombination. However, the specific pathway and mechanistic rationale of Ag metal in FOR have been studied very little. The main challenge to this method lies in preparing a highly dispersed Ag electrocatalyst.

Herein, we report a facile method with which nickel foam (NF) can be modified with L-arginine and anchor silver nanoparticles (AgNP) and then used for bipolar H_2 production in alkaline media (Fig. 1). As reported previously, L-arginine is an amphoteric chelating agent that can maintain its compositional homogeneity during the preparation of metal precursors [1,31]. Moreover, an NH_3^+ moiety used as a tether can orientate the growth of metal ions from the medium, achieving deliberate modification of the surface of the catalyst [32–34]. The AgNPs become uniformly dispersed on the surface of the NF, where they serve as active sites for FOR, attaining near 100% Faradaic efficiency at low overpotentials. *In situ* Raman spectroscopy was used to probe the Ag-FOR interface and ascertain the role of Ag in promoting the dehydrogenation of formaldehyde. Density functional theory (DFT) calculations confirmed the exothermic nature of the reaction process on Ag and shed light on the mechanism. We also demonstrated the potential of AgNPs-anchored NF as a bifunctional catalyst for bipolar hydrogen production.

2. Results and discussion

2.1. Characterization of materials

The surface structure and metal element distribution of materials were monitored by scanning electron microscopy (SEM). $Ag_{d,r}/NF$ treated with L-arginine has irregular cracks on its surface, exposing the internal nickel foam and enhancing the electrocatalytic performance of the anchored Ag nanoparticles (Fig. 2a and 2b). $Ag_{d,r}/NF$ also had tiny nanoparticles of 1–2 nm, covering the entire surface of the nickel foam substrate (Fig. 2c). Elemental mapping analysis verified the uniform dispersion of Ag nanoparticles on the surface of the substrate (Fig. 2d). In contrast, raw Ag/NF samples had aggregated Ag nanoparticles with less controlled size and dispersion (Fig. S2). The L-arginine treatment etched the nickel foam surface and controlled the size and dispersion of the Ag nanoparticles. The designed $Ag_{d,r}/NF$ catalyst had smaller and more distributed Ag nanoparticle active sites, and, in formaldehyde electrocatalytic oxidation, outperformed Ag/NF with the same amount

of Ag ions.

The oxidation state of individual elements in the material is investigated by X-ray photoelectron spectroscopy (XPS), X-ray diffraction (XRD) and transmission electron microscopy (TEM). The XPS spectrum of the $Ag_{d,r}/NF$ catalyst, shown in Fig. 3a, indicates the presence of Ni, O and Ag. Fine spectral fitting was done for these three elements. The 1 s orbital spectrum of O has distinct deconvolution peaks at 529.38 and 531.35 eV, corresponding to lattice oxygen and oxygen vacancies (Fig. 3b). The presence of oxygen suggests that the more active metallic Ni is not fully reduced to the zero-valent state by a high-temperature reduction in the Ar/H_2 atmosphere. However, the Ag active sites appear to have been reduced to zero-valent, as confirmed by fitting the Ag 3d orbital fine spectrum. In Fig. 3c, the two prominent absorption peaks in the $Ag_{d,r}/NF$ catalyst can be assigned to Ag^0 [35]. Moreover, a noticeable chemical shift is observed in the XPS peaks of $Ag_{d,r}/NF$ compared to Ag_d/NF before and after reduction in the Ar/H_2 atmosphere, with a binding energy decrease of about 0.15 eV (Fig. 3c). It indicates the complete reduction of $Ag_{d,r}/NF$ in the Ar/H_2 atmosphere. Analysis of the oxidation states of Ni in $Ag_{d,r}/NF$ and Ag_d/NF reveals that Ni exists mainly as Ni^0, Ni^{2+} and Ni^{3+} in both catalysts [36–39]. The proportion of Ni^0 is found to have increased significantly in the $Ag_{d,r}/NF$ material after reduction in the Ar/H_2 atmosphere (Fig. 3d).

$Ag_{d,r}/NF$ and Ag_d/NF are characterized by XRD to determine the crystal phase information of the metal materials in the catalyst. Fig. 3e shows the results, in which the peaks can be assigned to Ni (PDF#04–0850) and Ag (PDF#04–0783). Both samples exhibit diffraction peaks at 44.5° for Ni(111) and 44.3° for Ag(200), which is consistent with the lattice spacing of Ni(111) at 0.205 nm observed in TEM and the lattice spacing of Ag(200) at 0.204 nm (Fig. 3f). This suggests that the central crystal plane of Ag nanoparticles in the catalyst is Ag (200). Furthermore, we are curious whether the surface modification with L-arginine would alter the intrinsic crystal structure of NF. XRD results indicate that L-arginine only affected the surface of NF without changing its inherent lattice information, which remained consistent with Ni (PDF#04–0850) (Fig. S3).

2.2. Electrocatalytic performance

We compare the performance of $Ag_{d,r}/NF$ with other contrast samples (Ag/NF, Ag_d/NF, Ag_r/NF, and $Ag_{d,r}/CC$) as working electrodes in 1 M KOH + 1 M HCHO for formaldehyde electrocatalytic oxidation (Fig. 4a). The results show that except for Ag_r/NF, the other four catalysts have a noticeable current increase at 0.3–0.4 V. This is due to the insufficient growth of Ag nanoparticles on NF substrate in Ag/NF without L-arginine surface modification and Ar/H_2 reduction, which prevents the FOR reaction. Thus, we infer that L-arginine surface modification on NF and Ar/H_2 reduction significantly improves the catalytic performance of the catalyst for FOR. Moreover, we observe that $Ag_{d,r}/NF$ has the lowest onset potential for FOR, and the current increases rapidly without any apparent decay in the growth rate after the reaction starts. In contrast, the other three contrast catalysts (Ag_d/NF, Ag_r/NF, and $Ag_{d,r}/CC$) significantly decrease current density when the current density reaches 50–100 mA cm^{-1}. This is due to the insufficient Ag content on the surface, which reduces current density after the FOR reaction sites are saturated. The Tafel slopes of the five catalysts are consistent with the previous observations (Fig. 4b). $Ag_{d,r}/NF$ has the lowest onset potential for the reaction at about 0.23 V. Furthermore, it has the lowest slope of 92.6 mV dec^{-1}, indicating the fastest current increase compared to other contrast catalysts.

We also compare the LSV curves in 1 M KOH + 1 M HCHO and 1 M CH_3OH to minimize the possible influence of methanol stabilizers in the formaldehyde solution on the experimental results (Fig. 4c). The results show that the $Ag_{d,r}/NF$ catalyst starts the FOR at an onset potential of 0.23 V. On the other hand, the onset potential for the methanol oxidation reaction (MOR) is 1.30 V. Therefore, the $Ag_{d,r}/NF$ catalyst starts the MOR reaction only slightly before the OER. Moreover, it is essential to
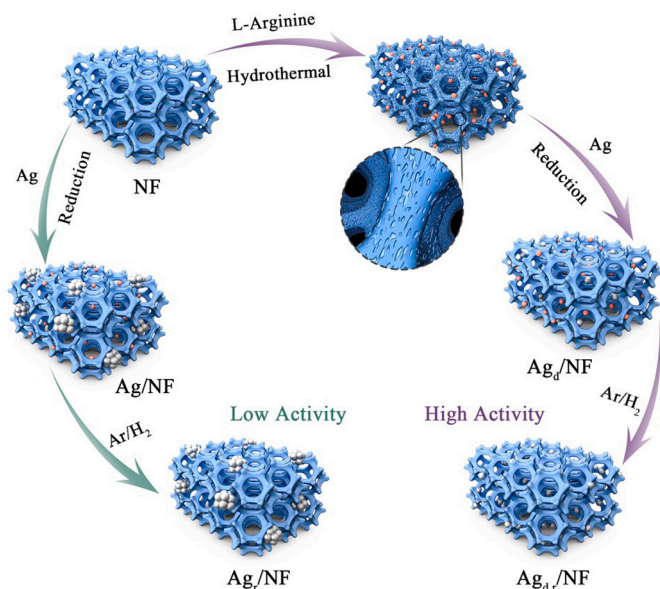

Fig. 1. Schematic illustration of L-arginine etched NF strategy for the design of a new Ag electrocatalyst in bipolar hydrogen production.
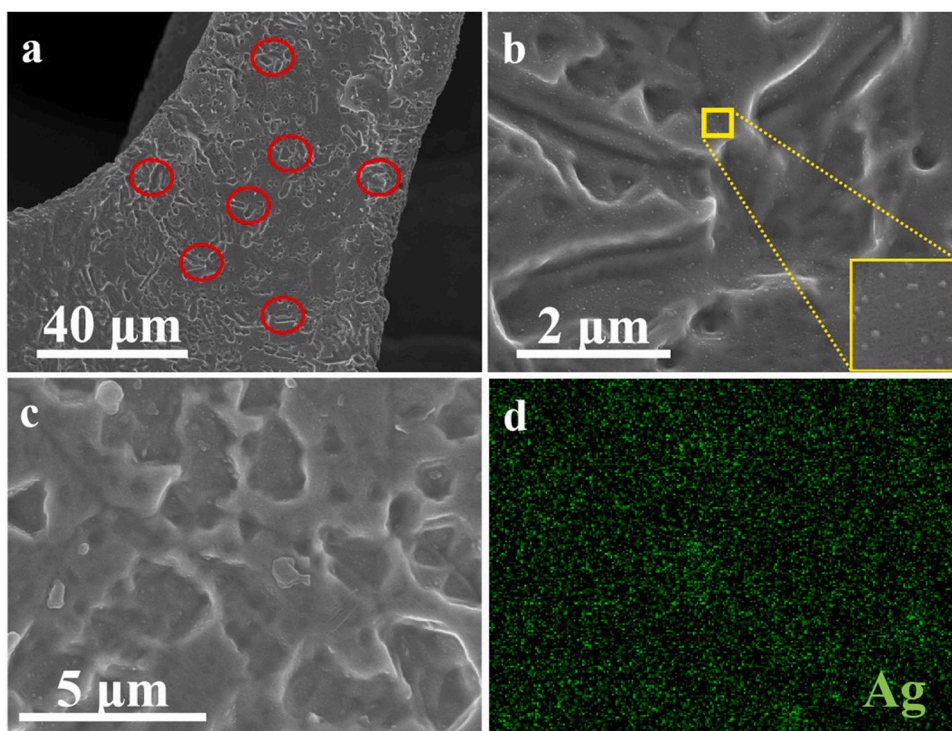
Fig. 2. **(a-c)** SEM images of Ag$_{d,r}$/NF and **(d)** EDX mapping of part **(c)**.
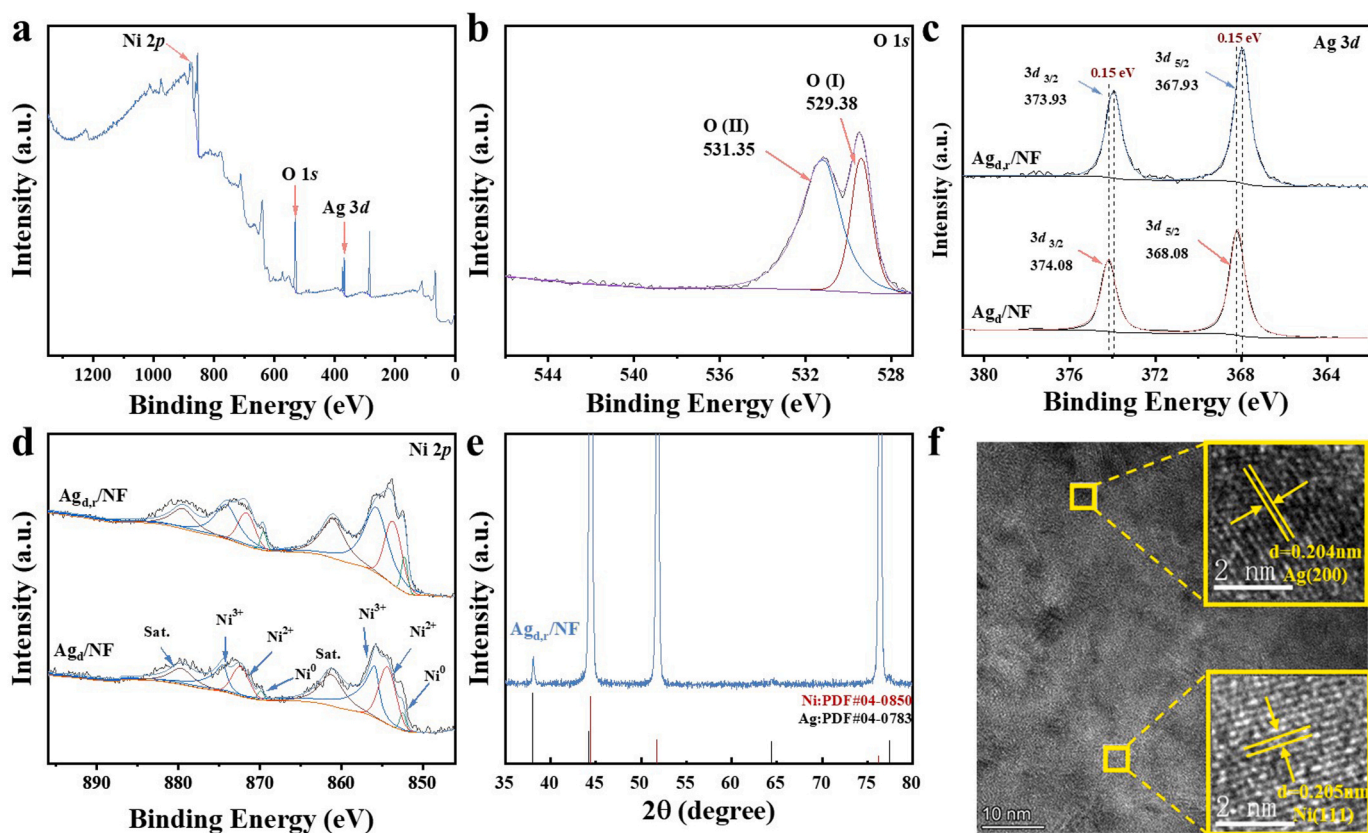
Fig. 3. **(a)** XPS analysis of Ag$_{d,r}$/NF. **(b)** XPS spectra of O 1s of Ag$_{d,r}$/NF catalyst. **(c)** XPS spectra of Ag 3d of Ag$_{d,r}$/NF and Ag$_d$/NF catalyst. **(d)** XPS spectra of Ni 2p of Ag$_{d,r}$/NF and Ag$_d$/NF catalyst. **(e)** XRD image of Ag$_{d,r}$/NF catalyst. **(f)** TEM image of Ag$_{d,r}$/NF.
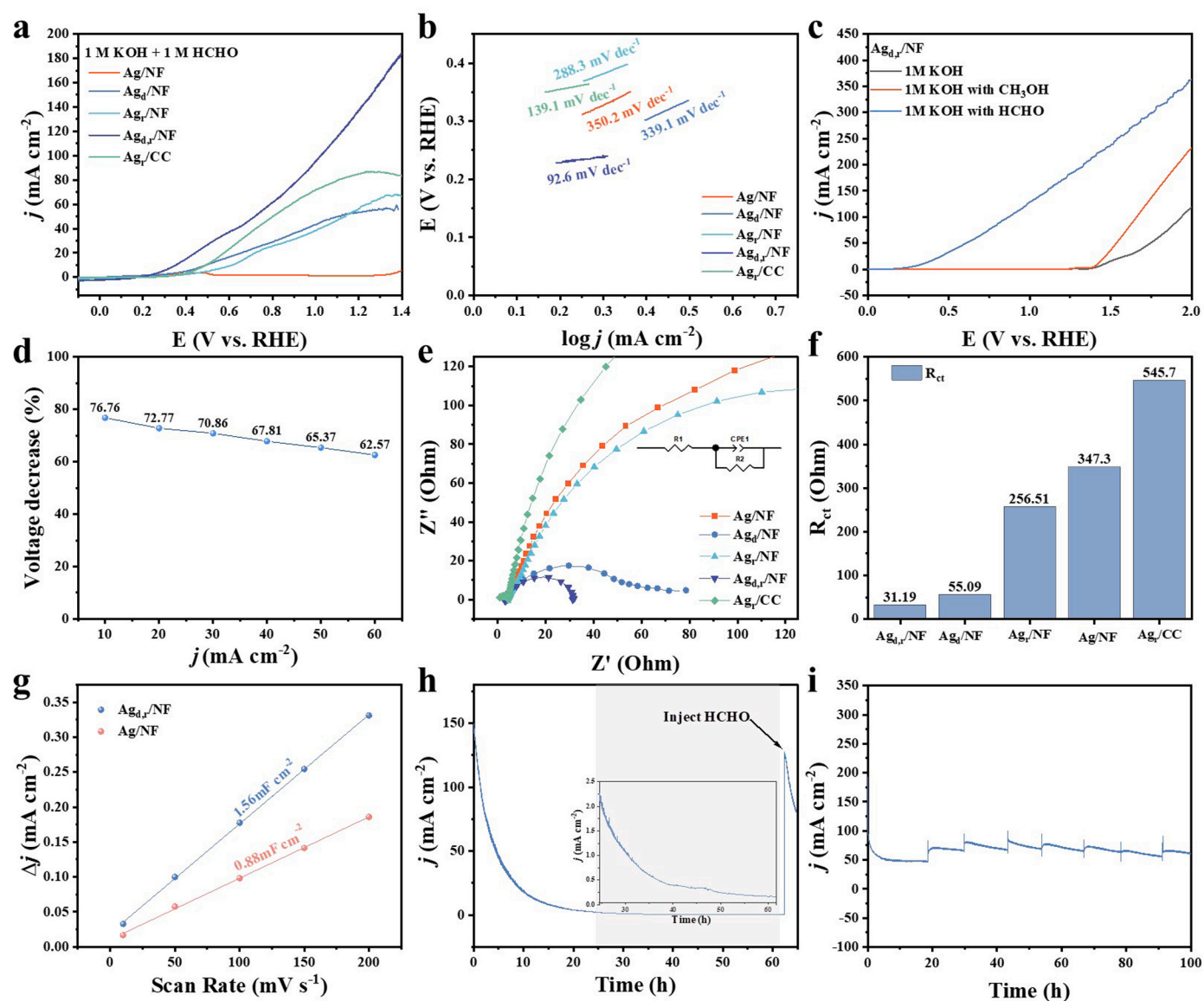
Fig. 4. (a) LSV curves of Ag/NF, Ag$_d$/NF, Ag$_r$/NF, Ag$_{d,r}$/NF, and Ag$_r$/CC for FOR in 1 M KOH with 1 M HCHO at a scan rate of 5 mV s^{-1}. (b) The corresponding Tafel plots are shown for the cases above. (c) The LSV curves of Ag$_{d,r}$/NF in different solutions. (d) The energy-saving performance of the Ag$_{d,r}$/NF catalyst at various current densities. (e) and (f) The charge transfer resistance of different catalysts at the onset potential of FOR. (g) The capacitance comparison diagram between Ag/NF and Ag$_{d,r}$/NF is presented. (h) displays the potentiostatic method curve of Ag$_{d,r}$/NF at a potential of 1.35 V for 60 h. (i) The 100-hour stability experiment of Ag$_{d,r}$/NF conducted under a potentiostatic method in a flowing electrolyte cell system.

note that at the 1.30 V potential, the current density for FOR is more than 200 mA cm^{-1}, implying that within the tested range of 100 mA cm^{-1} current density, FOR is unaffected by MOR interference.

The catalytic role of Ag$_{d,r}$/NF for formaldehyde oxidation in the alkaline system was further elucidated by analyzing the LSV curves with and without formaldehyde (Fig. 4c and S8). The results show that in the presence of formaldehyde, the FOR begins at a potential of 0.35 V. A comparison with the group without formaldehyde shows that both cases have positive current growth at 0.35 V. This can be attributed to the oxidation state change, metallic Ag^0 losing one electron to produce Ag$^+$, resulting in the change in current. It can be inferred that the initial step of Ag involvement in FOR is an electron loss from Ag^0 at the anode surface, followed by the binding of the resulting Ag$^+$ with a formaldehyde molecule to facilitate the subsequent catalytic oxidation. After a series of catalytic steps, Ag^0 is regenerated from Ag$^+$. It is noteworthy that coupling the FOR with the HER significantly reduces energy consumption compared to traditional HER and OER processes. At a current density of 10 mA cm^{-2}, an energy-saving efficiency of 76.76% can be

achieved. Although the energy-saving efficiency decreases slightly with increasing current density, it still is 62.57% at a current density of 60 mA cm^{-2} (Fig. 4d). In addition, we determined the loading amount of Ag using inductively coupled plasma atomic emission spectrometry (ICP-OES), obtaining the results shown in **Tab. S1**. The data reveal that Ag$_{d,r}$/NF can provide a current density of 2.56 A mg$_{Ag}^{-1}$, which surpasses the 1.5 A mg^{-1} Ag typically achieved by most commercially available catalysts.

Charge transfer resistance (Rct) is a critical indicator describing the electron transfer resistance at the reaction interface. We measure the corresponding Rct of Ag$_{d,r}$/NF and other control catalysts at the onset potential of FOR (Figs. 4e and 4f). The results indicate that Ag$_{d,r}$/NF possesses the smallest Rct value, suggesting it exhibits the fastest electron transfer rate during oxidation reactions at the catalytic interface. It implies that electrons can swiftly transfer between the catalyst surface and the electrolyte, endowing exceptionally high FOR reaction activity. Based on the cyclic voltammetry (CV) curves estimated from Fig. S9a and S9b, an electrical double-layer capacitor (C_{dl}) can be used to

evaluate the electrochemical active surface area (ECSA). As shown in Fig. 4**g**, the results revealed that the C_{dl} of Ag/NF is 0.88 mF cm^{-2}, much lower than the capacitance of the modified Ag$_{d,r}$/NF electrode, which was 1.56 mF cm^{-2}. This suggests that surface modification effectively enhances the active surface area, improving its catalytic performance.

Long-term stability is crucial for the practical utilization of electrocatalysts. Acordingly, a 60 h stability test of Ag$_{d,r}$/NF was conducted using the amperometric i-t curve method at a potential of 1.35 V (Fig. 4**h**). The results obtained show that as the substrate (HCHO) concentration decreases continuously, the current falls from 150 mA and gradually approaches 0 mA after 20 h. Zooming in, it can be seen that the current in the system stays around 3 mA during the 20–60 h period, showing that the FOR reaction is continuing without significant decay. At hour 60, the current returns to 150 mA upon adding an equivalent amount of HCHO solution. This demonstrates that Ag$_{d,r}$/NF maintains stable catalytic performance for the FOR over 60 h with no significant decline. We monitor the formaldehyde concentration in the solution and observe a rapid decrease in the initial stages of the reaction (Fig. S10). However, the formaldehyde concentration changes more slowly between 20 and 60 hours. We infer that at a potential of 1.35 V, other competing reactions, such as MOR or OER, start to take place as the formaldehyde concentration drops, but with very low current densities. This also accounts for the constant current density of about 3 mA during the 20–60 hours. To ensure the stability of FOR testing, we lower the reaction potential to 1.0 V, which reduces the interference from competing reactions. Moreover, we use a flow-through electrolysis cell to keep the formaldehyde concentration steady, avoiding interference from concentration variations during testing. We perform stability tests for up to 100 hours under a flowing electrolyte system (Fig. 4**i** and **S11**).

With the stable formaldehyde concentration in the electrolyte, we conduct constant potential experiments with a current of 50–100 mA and replace the electrolyte every 12 hours. The results show no noticeable current decay over 100 hours, demonstrating the outstanding stability of the catalyst's FOR performance. After the stability test, we characterize Ag$_{d,r}$/NF by SEM and XRD (Fig. S12). The SEM results show nanoparticle aggregation on the catalyst surface due to the long-term operation at high current density. The XRD results confirm that the catalyst's lattice composition remains unchanged after the prolonged FOR catalytic reaction.

The product information and electron utilization in the FOR&HER bipolar system were further understood after analysis of the reactions in a dual electrolysis cell arrangement. Ag$_{d,r}$/NF and Ag/NF were applied simultaneously as the anode and cathode to study the bifunctional properties (Fig. S13). By comparing the LSV curves, it was found that Ag$_{d,r}$/NF for FOR&HER required only 1.09 V of potential change (ΔE) to drive the current density from −50 to +50 mA cm^{-2}. In contrast, the unmodified Ag/NF required ΔE = 1.80 V to achieve the exact current density change (Fig. 5**a**). This confirms the enhancement of catalytic performance by the surface modification of Ag$_{d,r}$/NF. Many bubbles were generated on the anodic FOR electrode surface, and differential electrochemical mass spectrometry (DE-MS) was used to analyze the products on the surface of the FOR electrode in 1 M HCHO + 1 M NaOD in D$_2$O (Fig. 5**b** and **S14**). The results showed no significant signals were collected from the electrode surface without an applied voltage. However, when a voltage of 0.3 V was used, a signal at $m/z = 2$ was detected, indicating the voltage-dependent generation of H$_2$ on the electrode surface.

The three channels at $m/z = 3$, 4, and 44 were also monitored, and no
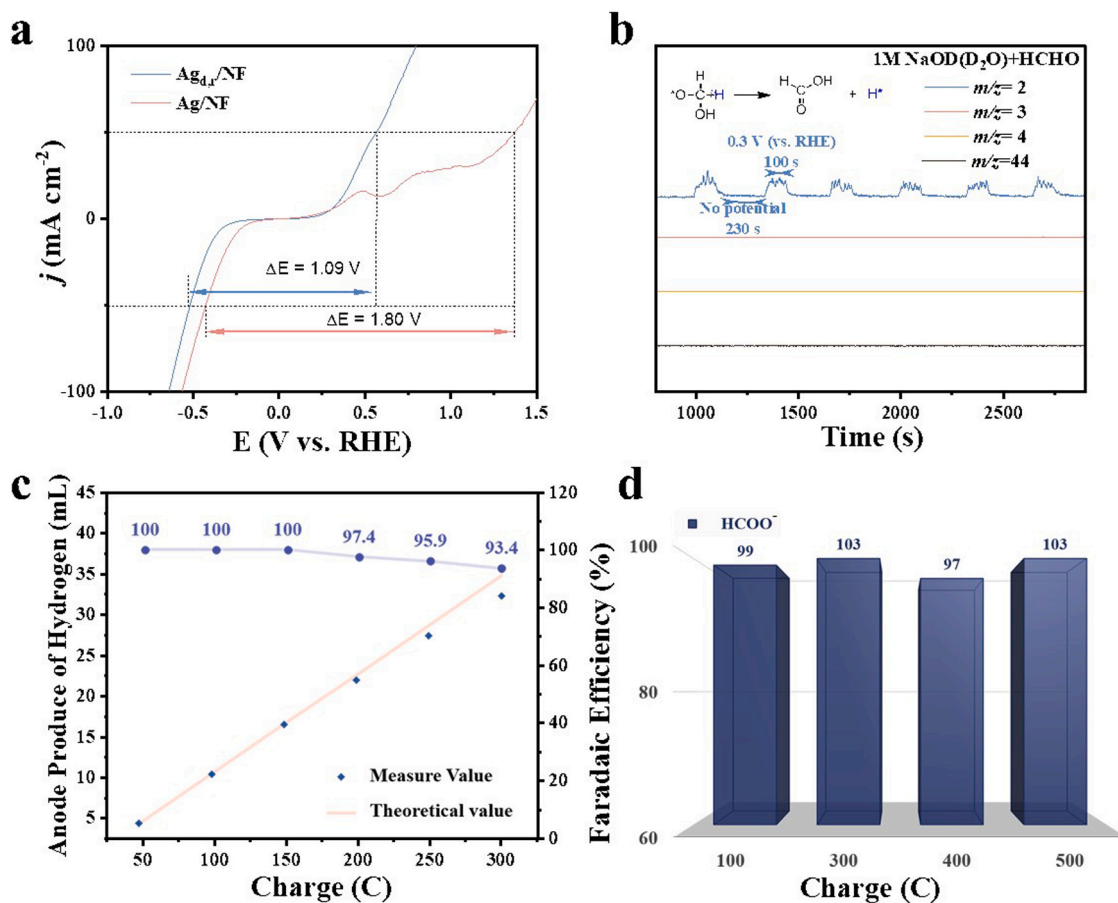
Fig. 5. **(a)** CV curves of Ag/NF and Ag$_{d,r}$/NF for HCHO oxidation in 1 M KOH with 1 M HCHO at a scan rate of 5 mV s^{-1}, **(b)** *In situ* DE-MS of 1 M HCHO electrooxidation in 1 M NaOD on Ag$_{d,r}$/NF, **(c)** Comparison of H$_2$ collected from experimental measurements and theoretical calculations. **(d)** ion-chromatography of the diluted electrolyte after electrocatalytic FOR catalyzed by Ag$_{d,r}$/NF.

significant signals were detected upon application of the pulsed voltage, indicating that the FOR reaction system generated no HD, D_2, or CO_2 as products. This shows that in the $Ag_{d,r}$/NF-catalyzed FOR, the H atoms are both from HCHO, and HCHO is oxidized to H_2 and formate rather than CO_2. To further eliminate the potential influence of formaldehyde's self-disproportionation in an alkaline solution, we conduct two experiments: a) Adding $Ag_{d,r}$/NF electrocatalyst to 1 M KOH+1 M HCHO electrolyte without applying additional voltage. We monitor changes in formaldehyde concentration using ^{1}H NMR over 0–3 hours (Fig. S15). b) No catalyst or voltage is applied to the same electrolyte. We monitor changes in formaldehyde concentration over 0–3 hours. The results indicate no significant decrease in formaldehyde concentration. Thus, it demonstrates that formaldehyde oxidation and hydrogen generation reactions require externally applied voltage and electrocatalyst. Hydrogen production from formaldehyde oxidation can proceed through two pathways: a single-electron pathway, HCHO + $2OH^-$ → $HCOO^-$ + H_2O + 1/2 H_2 + e^- or a double-electron pathway, HCHO + $3OH^-$ → $HCOO^-$ + 2 H_2O + $2e^-$. The DE-MS results suggest that a single-electron mechanism is more likely to match the reaction performance. The gas-phase products were collected and measured to determine their relationship with the number of electrons consumed. It was confirmed that the $Ag_{d,r}$/NF-catalyzed FOR follows the single-electron type pathway (Fig. 5c). The Faradaic efficiency for hydrogen production at the anode was calculated to be nearly 100%. The volume of hydrogen gas collected from the cathode was measured using the same method, and the Faradaic efficiency was also estimated to be close to 100% (Fig. S16). However, as the number of input electrons increased, the Faradaic efficiency decreased, possibly due to the decreasing concentration of the formaldehyde substrate. Ion chromatography (IC) analysis of the liquid-phase products in the FOR reaction showed that formaldehyde was oxidized to formate ions with a Faradaic efficiency close to 100% (Fig. 5d and S17). The hydrogen production at the cathode for the HER was collected and measured, and showed that $Ag_{d,r}$/NF also had a Faradaic efficiency close to 100%. Therefore, the Agd,r/NF electrocatalyst has bifunctional characteristics that allow their simultaneous application in FOR&HER.

2.3. The FOR mechanism elucidated by in-situ Raman spectroscopy and density functional theory (DFT) calculations

Using *in situ* Raman spectroscopy and DFT calculations, we elucidated the reaction process of formaldehyde (HCHO) on an Ag catalyst, confirmed the presence of HCOOH* intermediates and identified two distinct oxidation mechanisms. The high dispersion of Ag nanoparticles on the NF surface (Fig. S18) precluded the detection of large aggregates. To prevent laser-induced damage to the Ag particles, we applied a low laser intensity (1%) and targeted regions with higher Ag density. We acquired Raman spectra at potentials ranging from −0.1–1.4 V with a 50 mV increment and amplified the signal by extending the measurement time and increasing the number of acquisitions (Fig. 6). The Raman spectra showed a marked decline in the Ag-OH peak at 400–500 cm^{-1} with increasing potential, while the Ag-O peak at 650–700 cm^{-1} [40,41] appeared at 0.35 V and became more prominent with a further increase in the potential. This indicates that Ag begins interacting with the O atom in HCHO at or above 0.35 V, facilitating subsequent reactions. A clear O-C-O peak was also detected at 1300–1400 cm^{-1} [42–44] that rose as the potential increased, indicating the emergence of HCOOH-forming intermediates. From Raman spectroscopy data, it can be inferred that OH^- ions in the solution first adsorb onto the surface of Ag. With increased potential, formaldehyde molecules also adsorb onto the Ag surface (beyond 0.3 V). Additionally, the reaction products of electrocatalysis should primarily include the OCO structure. Combining this information, we propose two reaction pathways and discuss the reaction energy levels of these pathways through DFT calculations.

The FOR pathway on the Ag (200) surface was investigated by DFT calculations. Fig. 7a and S19 show that in Path 1, the active metal Ag interacts with HCHO and HO* through an electrochemical process, undergoes C-H bond breaking (TS_1) and H-H bond formation (TS_2) and produces HCOOH* with H_2. The specific reaction mechanism can be outlined as follows: 1. HCHO + OH^- + Ag^+ → $H_2C(O)OH$-Ag; 2. $H_2C(O)OH$-Ag → H-Ag-HCOOH → Ag-HCOOH + 1/2 H_2. In the second pathway (Fig. S20), the active metal silver (Ag) forms a surface complex with HO* from the alkaline medium, which acts as the active site for the reaction.
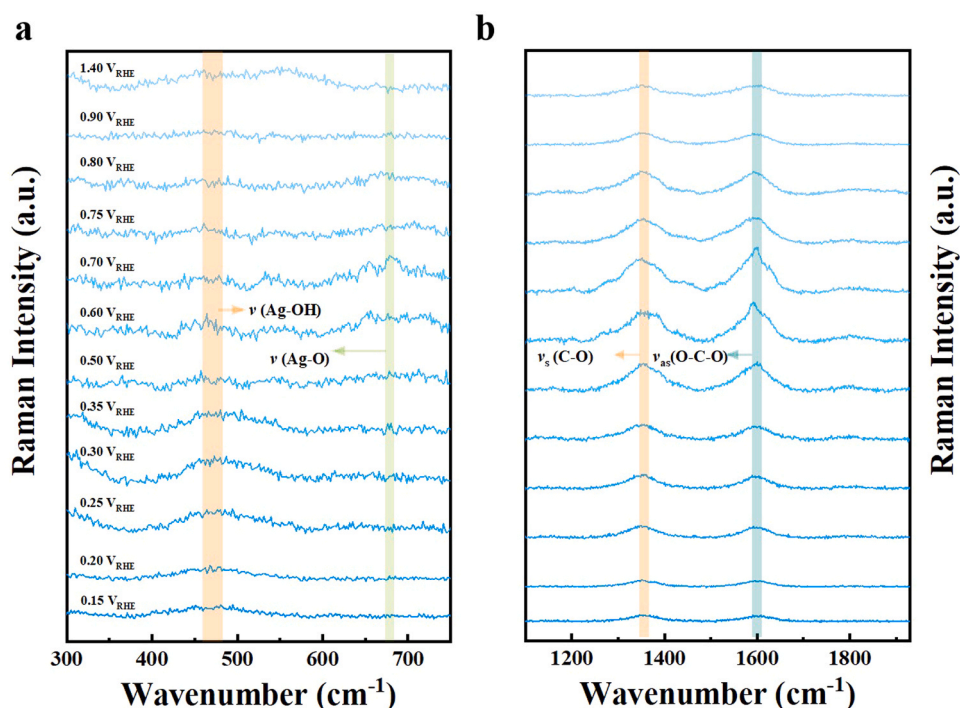

a

b

Fig. 6. *In*-situ Raman spectroscopy of the reaction process on the Ag catalyst surface.
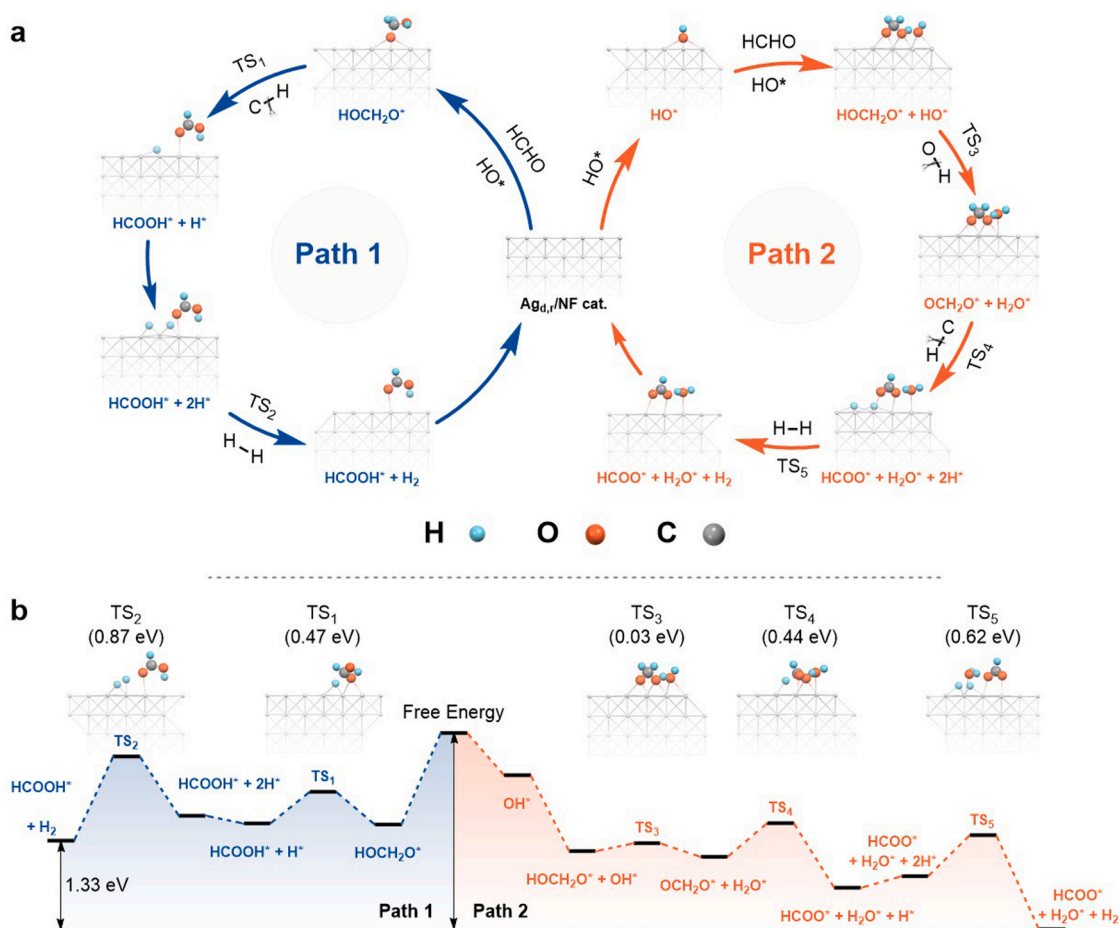
Fig. 7. (a) The reaction pathway on Ag-based catalysts based on DFT calculation, **(b)** Free energy profiles on the Ag surface of Path 1 and Path 2.

Meanwhile, HOCH$_2$O*, produced by combining HO* and HCHO in the solution, also adsorbs on the catalyst surface. It undergoes O-H bond breaking (TS$_3$), C-H bond breaking (TS$_4$), and H-H bond formation (TS$_5$), generating HCOO* + H$_2$O* + H$_2$. The specific reaction mechanism can be outlined as follows: 1. OH$^-$ + Ag$^+$ →Ag-OH; 2. Ag-OH + HCHO →H$_2$C(O)OH-Ag; 3. H$_2$C(O)OH-Ag + OH$^-$ + Ag$^+$ → [H$_2$COO-Ag] + H$_2$O +Ag; 4. [H$_2$COO-Ag] → HCOO-Ag + 1/2 H$_2$. Path 2 has an additional O-H bond-breaking step. Fig. 7b illustrates the free energy barrier variation for Path 1 and Path 2. Both pathways are exothermic with ΔG < 0. Path 1 has two main energy barriers, TS$_1$ and TS$_2$ (0.47 and 0.87 eV), and reaction energies of −1.33 and −1.58 eV, respectively. Path 2, on the other hand, has TS$_3$, TS$_4$ and TS$_5$ with free energy barriers of 0.03, 0.44, and 0.62 eV, and reaction energies of −2.14, −2.66, and −2.92 eV, respectively. The dynamics and energetics suggest that Path 2, which favors the FOR reaction on the Ag (200) surface, is more favorable for the FOR reaction because the intermediates are more stable. In summary, the computational studies demonstrate the general mechanism of the HER and FOR process, and clarify the role of added KOH.

3. Conclusion

In conclusion, this work presents a promising electrocatalyst, Ag$_{d,r}$/NF, that facilitates FOR&HER at low potentials. After surface etching, the size and dispersion of Ag nanoparticles on the NF substrate can be effectively controlled, leading to an increased active surface area. The catalyst shows long-term stability even at high current densities. DE-MS analysis shows that Ag$_{d,r}$/NF efficiently converts formaldehyde into formate ions, with only hydrogen derived from formaldehyde. DFT calculations confirm the unique advantages of Ag in driving the FOR and

provide detailed insights into the possible reaction pathways. These findings offer new design strategies for electrodes in efficient H$_2$ production.

CRediT authorship contribution statement

Yan Zhang: Writing – original draft, Methodology, Formal analysis, Data curation. **Jindong Wu:** Writing – original draft, Data curation. **Jiean Chen:** Writing – review & editing, Supervision, Project administration, Funding acquisition. **Xinrui Zhu:** Software, Investigation. **Zhi Ren:** Validation, Software.

Declaration of Competing Interest

The authors declare that they have no known competing financial interests or personal relationships that could have appeared to influence the work reported in this paper.

Data Availability

No data was used for the research described in the article.

DFT calculation.

Appendix A. Supporting information

Supplementary data associated with this article can be found in the online version at doi:10.1016/j.apcatb.2024.124093.

References

[1] S. Jiang, J. Yang, S. Zhai, L. Zhang, R. Tu, T. Yu, D. Zhai, L. Sun, W. Deng, G. Ren, Ambient hydrogen storage and release using CO_2 and an l-arginine-functionalized PdAu catalyst via pH control, ACS Catal. 12 (2022) 14113–14122.

[2] H. Chen, Y. Zheng, J. Li, L. Li, X. Wang, AI for nanomaterials development in clean energy and carbon capture, utilization and storage (CCUS), ACS Nano 17 (2023) 9763–9792.

[3] J. Wu, N. Li, Impact of components number selection in truncated Gaussian mixture model and interval partition on wind speed probability distribution estimation, Sci. Total Environ. 883 (2023) 163709.

[4] S. Kraemer, J. Moens, M. Athanasakis-Kaklamanakis, S. Bara, K. Beeks, P. Chhetri, K. Chrysalidis, A. Claessens, T.E. Cocolios, J.G.M. Correia, H. Witte, R. Ferrer, S. Geldhof, R. Heinke, N. Hosseini, M. Huyse, U. Koster, Y. Kudryavtsev, M. Laatiaoui, R. Lica, G. Magchiels, V. Manea, C. Merckling, L.M.C. Pereira, S. Raeder, T. Schumm, S. Sels, P.G. Thirolf, S.M. Tunhuma, P. Van Den Bergh, P. Van Duppen, A. Vantomme, M. Verlinde, R. Villarreal, U. Wahl, Observation of the radiative decay of the ^{229}Th nuclear clock isomer, Nature 617 (2023) 706–710.

[5] Z. Chen, S. Yun, L. Wu, J. Zhang, X. Shi, W. Wei, Y. Liu, R. Zheng, N. Han, B.J. Ni, Waste-Derived catalysts for water electrolysis: circular economy-driven sustainable green hydrogen energy, Nanomicro Lett. 15 (2022) 4.

[6] P. Sharma, M. Sharma, M. Dearg, M. Wilding, T.J.A. Slater, C.R.A. Catlow, Cd/Pt precursor solution for Solar H_2 production and in situ photochemical synthesis of Pt single-atom decorated CdS nanoparticles, Angew. Chem. Int. Ed. 62 (2023) e202301239.

[7] R. Cortright, R. Davda, J. Dumesic, Hydrogen from catalytic reforming of biomass-derived hydrocarbons in liquid water, Nature 418 (2002) 964–967.

[8] B. Rausch, M.D. Symes, G. Chisholm, L. Cronin, Decoupled catalytic hydrogen evolution from a molecular metal oxide redox mediator in water splitting, Science 345 (2014) 1326–1330.

[9] R.D.L. Smith, M.S. Prévot, R.D. Fagan, Z. Zhang, P.A. Sedach, M. Kit Jack Siu, S. Trudel, C.P. Berlinguet, Science 340 (2013) 60–63.

[10] M.E. Ivanova, R. Peters, M. Muller, S. Haas, M.F. Seidler, G. Mutschke, K. Eckert, P. Rose, S. Calnan, R. Bagacki, R. Schlatmann, C. Grosselindemann, L.A. Schafer, N. H. Menzler, A. Weber, R. van de Krol, F. Liang, F.F. Abdi, S. Brendelberger, N. Neumann, J. Grobbel, M. Roeb, C. Sattler, I. Duran, B. Dietrich, M.E. C. Hofberger, L. Stoppel, N. Uhlenbruck, T. Wetzel, D. Rauner, A. Hecimovic, U. Fantz, N. Kulyk, J. Harting, O. Guillon, Technological pathways to produce compressed and highly pure hydrogen from solar power, Angew. Chem. Int. Ed. 62 (2023) e202218850.

[11] H. Zhao, Z.Y. Yuan, Progress and perspectives for solar-driven water electrolysis to produce green hydrogen, Adv. Energy Mater. 13 (2023) 2300254.

[12] D.R. Kauffman, D. Alfonso, D.N. Tafen, J. Lekse, C. Wang, X. Deng, J. Lee, H. Jang, J.-s Lee, S. Kumar, C. Matranga, Electrocatalytic oxygen evolution with an atomically precise nickel catalyst, ACS Catal. 6 (2016) 1225–1234.

[13] F. Guo, T.J. Macdonald, A.J. Sobrido, L. Liu, J. Feng, G. He, Recent Advances in Ultralow-Pt-Loading Electrocatalysts for the Efficient Hydrogen Evolution, Adv. Sci. 10 (2023) e2301098.

[14] Y. Feng, X. He, M. Cheng, Y. Zhu, W. Wang, Y. Zhang, H. Zhang, G. Zhang, Selective adsorption behavior modulation on nickel selenide by heteroatom implantation and heterointerface construction achieves efficient Co-production of H_2 and formate, Small 19 (2023) e2301986.

[15] X. Qin, D. Kim, Y. Piao, Metal-organic frameworks-derived novel nanostructured electrocatalysts for oxygen evolution reaction, Carbon Energy 3 (2020) 66–100.

[16] S.-K. Geng, Y. Zheng, S.-Q. Li, H. Su, X. Zhao, J. Hu, H.-B. Shu, M. Jaroniec, P. Chen, Q.-H. Liu, S.-Z. Qiao, Nickel ferrocyanide as a high-performance urea oxidation electrocatalyst, Nat. Energy 6 (2021) 904–912.

[17] J. Li, Z. Guo, W. Zhang, J. Guo, K. Qu, W. Cai, Stable NiPt–Mo_2C active site pairs enable boosted water splitting and direct methanol fuel cell, Green. Energy Environ. 8 (2023) 559–566.

[18] X. Wu, Y. Zhang, Y. Yang, G. Fu, F. Si, J. Chen, M. Ahmad, Z. Zhang, C. Ye, J. Zhang, X.-Z. Fu, J.-L. Luo, Ni_2P with phosphorus vacancy supported Pt clusters for efficiently electrocatalytic co-production of hydrogen and value-added chemicals from methanol-water at low potential, Chem. Eng. J. 452 (2023) 139057.

[19] Z.-X. Ge, Y. Ding, T.-J. Wang, F. Shi, P.-J. Jin, P. Chen, B. He, S.-B. Yin, Y. Chen, Interfacial engineering of holey platinum nanotubes for formic acid electrooxidation boosted water splitting, J. Energy Chem. 77 (2023) 209–216.

[20] W. Jia, B. Liu, R. Gong, X. Bian, S. Du, S. Ma, Z. Song, Z. Ren, Z. Chen, Electronic Modulation Induced by Ni-VN Heterojunction Reinforces Electrolytic Hydrogen Evolution Coupled with Biomass Upgrade, Small 19 (2023) e2302025.

[21] C. Yang, C. Wang, L. Zhou, W. Duan, Y. Song, F. Zhang, Y. Zhen, J. Zhang, W. Bao, Y. Lu, D. Wang, F. Fu, Refining d-band center in $Ni_{0.85}Se$ by Mo doping: A strategy for boosting hydrogen generation via coupling electrocatalytic oxidation 5-hydroxymethylfurfural, Chem. Eng. J. 422 (2021) 130125.

[22] G. Qian, J. Chen, W. Jiang, T. Yu, K. Tan, S. Yin, Strong electronic coupling of CoNi and N-doped-carbon for efficient urea-assisted H_2 production at a large current density, Carbon Energy 6 (2023) e368.

[23] M. Song, Z. Zhang, Q. Li, W. Jin, Z. Wu, G. Fu, X. Liu, Ni-foam supported Co(OH)F and Co–P nanoarrays for energy-efficient hydrogen production via urea electrolysis, J. Mater. Chem. A 7 (2019) 3697–3703.

[24] Z. Wang, G. Yang, P. Tian, K. Deng, H. Yu, Y. Xu, X. Li, H. Wang, L. Wang, Heterointerface engineering of Rh/Pd metallene for hydrazine oxidation-assisted energy-saving hydrogen production, J. Mater. Chem. A 11 (2023) 10222–10227.

[25] X. Liu, J. He, S. Zhao, Y. Liu, Z. Zhao, J. Luo, G. Hu, X. Sun, Y. Ding, Self-powered H (2) production with bifunctional hydrazine as sole consumable, Nat. Commun. 9 (2018) 4365.

[26] Y. Pan, Y. Li, C.-L. Dong, Y.-C. Huang, J. Wu, J. Shi, Y. Lu, M. Yang, S. Wang, Y. Zou, Unveiling the synergistic effect of multi-valence Cu species to promote formaldehyde oxidation for anodic hydrogen production, Chem 9 (2023) 963–977.

[27] G. Li, G. Han, L. Wang, X. Cui, N.K. Moehring, P.R. Kidambi, D.E. Jiang, Y. Sun, Dual hydrogen production from electrocatalytic water reduction coupled with formaldehyde oxidation via a copper-silver electrocatalyst, Nat. Commun. 14 (2023) 525.

[28] F. Si, J. Liu, Y. Zhang, B. Zhao, Y. Liang, X. Wu, X. Kang, X. Yang, J. Zhang, X.Z. Fu, J.L. Luo, Surface Spin Enhanced High Stable NiCo(2) S(4) for Energy-Saving Production of H(2) from Water/Methanol Coelectrolysis at High Current Density, Small 19 (2023) 2205257.

[29] H. Liu, N. Agrawal, A. Ganguly, Y. Chen, J. Lee, J. Yu, W. Huang, M. Mba Wright, M.J. Janik, W. Li, Ultra-low voltage bipolar hydrogen production from biomass-derived aldehydes and water in membrane-less electrolyzers, Energy Environ. Sci. 15 (2022) 4175–4189.

[30] H. Liu, J. Yu, Y. Chen, J. Lee, W. Huang, W. Li, Cu-Based Bimetallic Catalysts for Electrocatalytic Oxidative Dehydrogenation of Furfural with Practical Rates, ACS Appl. Mater. Interfaces 15 (2023) 37477–37485.

[31] W. Hong, M. Kitta, N. Tsumori, Y. Himeda, T. Autrey, Q. Xu, Immobilization of highly active bimetallic PdAu nanoparticles onto nanocarbons for dehydrogenation of formic acid, J. Mater. Chem. A 7 (2019) 18835–18839.

[32] Y. Namgung, J. Hong, A. Kumar, D.-K. Lim, S.-J. Song, One step infiltration induced multi-cation oxide nanocatalyst for load proof SOFC application, Appl. Catal. B 267 (2020) 118374.

[33] J. Feng, F. Wang, C. Wang, K. Li, X. Sun, P. Ning, Cu/HZSM-5 sorbent treated by NH(3) plasma for low-temperature simultaneous adsorption-oxidation of H(2)S and PH(3), ACS Appl. Mater. Interfaces 13 (2021) 24670–24681.

[34] Y. Zhang, J. Yang, Z. Yu, Y. Hou, R. Jiang, J. Huang, F. Yang, S. Yao, L. Gao, W. Tang, Modulating carbon-supported transition metal oxide by electron-giving and electron-absorbing functional groups towards efficient overall water splitting, Chem. Eng. J. 416 (2021) 129124.

[35] J. Wu, M. Wang, L. Dong, Y. Zhang, J. Shi, M. Ohyama, Y. Kohsaka, C. Zhu, H. Morikawa, Highly integrated, breathable, metalized phase change fibrous membranes based on hierarchical coaxial fiber structure for multimodal personal thermal management, Chem. Eng. J. 465 (2023) 142835.

[36] H. Wu, Q. Lu, J. Zhang, J. Wang, X. Han, N. Zhao, W. Hu, J. Li, Y. Chen, Y. Deng, Thermal shock-activated spontaneous growing of nanosheets for overall water splitting, Nanomicro Lett. 12 (2020) 162.

[37] L. Liao, D. Li, R. Xiang, Q. Dang, H. Zhou, Y. Zhang, S. Tang, F. Yu, Multi-site trifunctional hydrangea-like electrocatalysts for efficient industrial-level water/urea electrolysis with current density exceeding 1000 mA cm^{-2}, Sci. China Mater. 66 (2023) 3520–3529.

[38] W. Ma, D. Li, L. Liao, H. Zhou, F. Zhang, X. Zhou, Y. Mo, F. Yu, High-performance bifunctional porous iron-rich phosphide/nickel nitride heterostructures for alkaline seawater splitting, Small 19 (2023) e2207082.

[39] F. Zhang, Y. Liu, F. Yu, H. Pang, X. Zhou, D. Li, W. Ma, Q. Zhou, Y. Mo, H. Zhou, Engineering multilevel collaborative catalytic interfaces with multifunctional iron sites enabling high-performance real seawater splitting, ACS Nano 17 (2023) 2387–2398.

[40] T. Zhang, H. Shang, B. Zhang, D. Yan, X. Xiang, Ag/ultrathin-layered double hydroxide nanosheets induced by a self-redox strategy for highly selective CO_2 reduction, ACS Appl. Mater. Interfaces 13 (2021) 16536–16544.

[41] Y.J. Chen, Y.W. Chiang, M.H. Huang, Synthesis of diverse Ag_2O crystals and their facet-dependent photocatalytic activity examination, ACS Appl. Mater. Interfaces 8 (2016) 19672–19679.

[42] L. Diao, Y. Liu, F. Chen, H. Pan, D.Pd Lara, H. Liu, Y. Cheng, F. Luo, Improving the activity of electrochemical reduction of CO_2 to C1 products by oxidation derived copper catalyst, Mater. Rep.: Energy 3 (2023) 100180.

[43] W. Shan, R. Liu, H. Zhao, Z. He, Y. Lai, S. Li, G. He, J. Liu, In situ surface-enhanced Raman spectroscopic evidence on the origin of selectivity in CO_2 Electrocatalytic Reduction, ACS Nano 14 (2020) 11363–11372.

[44] X. Wang, C. Gao, J. Low, K. Mao, D. Duan, S. Chen, R. Ye, Y. Qiu, J. Ma, X. Zheng, R. Long, X. Wu, L. Song, J. Zhu, Y. Xiong, Efficient photoelectrochemical CO_2 conversion for selective acetic acid production, Sci. Bull. 66 (2021) 1296–1304.